2022 19th International Conference on Electrical Engineering, Computing Science and Automatic Control (CCE), Mexico City, Mexico, November 9-11, 2022

Capacitively Coupled Bandpass Filter Using Defected Ground Structure Featuring Shield Current Control

Jorge Aguilar-Torrentera
Electrical Engineering Faculty,
Universidad Autónoma de Nuevo León
Monterrey, Mexico
jorge.aguilart@uanl.mx

Giselle M. Galvan-Tejada
Communications Section, Department of Electrical Engineering,
Center for Research and Advanced Studies of IPN
Mexico City, Mexico
ggalvan@cinvestav.mx

José Ramón Rodríguez-Cruz
Electrical Engineering Faculty,
Universidad Autónoma de Nuevo León
Monterrey, Mexico
jrrcc68@gmail.com

***Abstract*— In this work, the design of capacitively coupled bandpass filter using a modified defected ground structure is presented. The unit-cell consists of a novel microstrip-type defect etched on the ground plane that retraces the shield current whereby regulating the magnetic current flow around its apertures at high frequencies. The equivalent circuit-model capacitance of such microstrip line makes available filter design having its bandpass frequency shifted to the higher side of the self-resonant frequency of constituent cells. The design approach is illustrated by a filter designed with bandpass at 10 GHz and its bandstop response is compared with that of a filter design with conventional capacitive-gap series resonators. It is seen that etched lattice size can be chosen to develop a specific inductance of the transmission line while keeping an allowable radiation loss. Besides, we analyze the effect of placing a separate solid metal in proximity with the ground plane of the microstrip line to evaluate the effectiveness of blinding moderate field leakage from the unit-cell. Numerical results obtained by three-dimensional electromagnetic simulation allows assessment of the proposed structures.**

Keywords*— *microwave bandpass filters, metallic shield, defected microstrip structure, electromagnetic bandgap component.

I. INTRODUCTION

For modern wireless communications systems and microwave applications, planar filters must satisfy stringent performance characteristics such as improved insertion loss, higher attenuation in the stop band and improved selectivity. Bandgap structures are attractive elements for filter design as microwave unit-cells demonstrate the properties of photonic bandgap (PBG) structure, which has a period to exhibit bandgap behavior or stopband effect defined by several lattice parameters [1]. A bandgap unit-cell is constructed with single or multiple defects etched either on the ground plane (defected ground structure, DGS [2]-[4]) or on the microstrip line (defected microstrip structure, DMS [5]-[6]). Microwave bandgap cells have given origin to high-performance lowpass and bandpass filters. Many filters utilize the slow-wave effect observed in the frequency range below the bandgap of constituent unit-cells, see for instance [2]-[10]. This behavior is associated with a circuit-model equivalence of the unit-cell that defines a dominant inductive effect below its attenuation pole. The most prominent disadvantage of DGS unit-cell is its high radiation. At higher frequencies, at which the associated equivalent capacitance is dominant, the DGS unit-cell exhibits larger field leakage through apertures. Hence, electric fields become scattered from the microstrip ground plane. At some extent, the lack of regulation of radiation loss is a motivation behind choosing the dominant inductive effect for filter design although large equivalent inductance may also result in high radiation loss even at frequencies below resonant.

When designing bandpass filters for communication multi-standard systems utilizing the same printed circuit board (PCB) backplane, higher attenuation in the stop band and improved isolation between channels must be accomplished [1]. Fig. 1 shows the application of the proposed filters based on DGS-unit cells tuned at different frequencies to create different bandpass channels. To achieve electromagnetic compatibility at the circuit level, unit-cells should be placed in close proximity with a metallic surface to isolate the bandpass filters. However, it is well-known that the DGS unit-cells radiate at high frequencies [2] and hence coupling energy due to excessive magnetic current around the defected ground appertures arises. Therefore, the implementation between unit cells will produce significant crosstalk between channels. Fig. 1 illustrates that the PCB implementation would present reactive and conductive type of couplings which will reduce isolation between channels with frequency. Therefore, minimizing shield current using the proposed structures becomes of fundamental importance for PCB design.

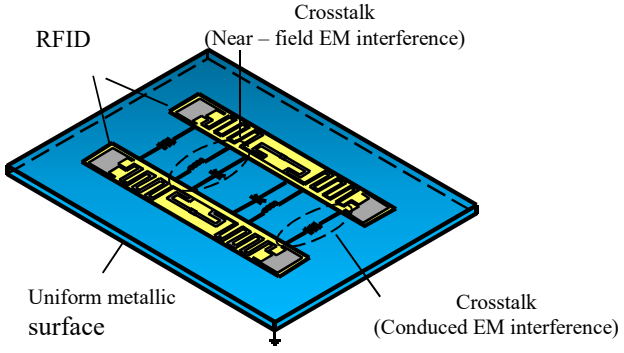

Fig. 1. L-Slot DGS unit-cell. 3D- view including separated grounding wall *a*), and dimensions of the backside view of the unit-cell *b*).

978-1-6654-5508-4/22/$31.00 ©2022 IEEE

This work reports for the first time a capacitively coupled bandpass filter (BPF) using a modified DGS structure, which was proposed and experimentally demonstrated in [11]. The harmful radiation from the ground plane is significantly diminished not only due to the miniaturization of the unit-cell but also as result of a substantial reduction of the magnetic current. The BPF is implemented with two unit-cell sections at the in-out ports to enhance the stopband performance of a single capacitive-gap resonator design. The filter provides attenuation and wider rejection band in the upper stopband improving frequency responses when compared with those of filter designs using conventional capacitive-gap resonators [12].

This paper is organized as follows: Section II details L-Slot unit-cells implementations and compares frequency responses with those of the conventional DGS pattern. EM performance of the L-Slot unit-cell is analyzed and the insertion of metallic wall in the EM environment of the microstrip line is evaluated in Section III. Section IV outlines a capacitively-coupled BPF implementation and its performance is assessed including a grounding plane. Final remarks are provided in Section V.

II. L-Slot Unit-Cells

The L-Slot DGS unit cell is shown in Fig. 2. "L" shaped-slot corresponds to the etched slots of length L_s bent in right-angle on the backside plane of a conventional DGS cell. This creates a microstrip-type defect along the unit-cell lattices to control return current. Originally, the defect was etched in the trace of the microstrip line to implement lowpass filters [5]-[6].

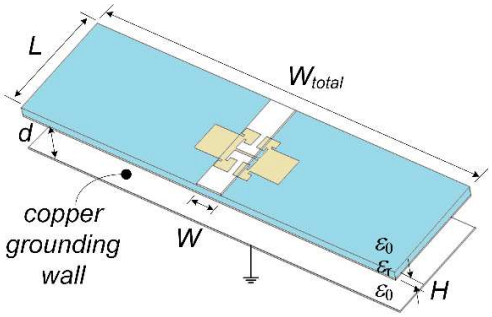

a)

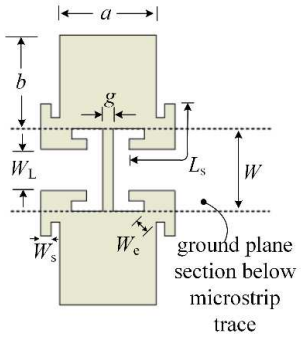

b)

Fig. 2. L-Slot DGS unit-cell. 3D- view including separated grounding wall *a*), and dimensions of the backside view of the unit-cell *b*).

Usually, DGS unit-cells introduce an equivalent dominant inductive effect to set the filter bandpass frequency below the self-resonance of the unit-cell, ω_0, being equal to $1/\sqrt{LC}$, where L and C are the equivalent circuit-model inductance and capacitance of the microstrip line. It is well known that the conventional DGS structure suffers from low capacitance [4], consequently; setting the center frequency requires earning magnetic current flow around the apertures to achieve a specific inductance. This entails to implement large lattice sizes resulting in unneglectable radiation from the grounding plane circuit area.

On the other hand, when the unit-cell presents an equivalent series capacitance (added chiefly by the slot head) above the central frequency, the field leakage will impact the bandpass response. Thus radiation from the backside of the microstrip line must be limited to an allowable rate. The microstrip-type defect becomes an attractive option for design. Fig. 3 allows comparing responses of the conventional dumbbell shaped DGS and those of the L-Slot. Smaller insertion loss and improved sharpness factor are evident. Fig. 4 depicts radiation rate showing diminished losses for the L-Slot DGS.

The unit-cell designs were carried out using substrate Duroid 5880® with 31-mil thick and dielectric constant $\varepsilon_r = 3.6$. Table I lists parameters of the unit-cell. Comsol™ V5.2 was used to simulate suspended microstrip lines surrounded by air.

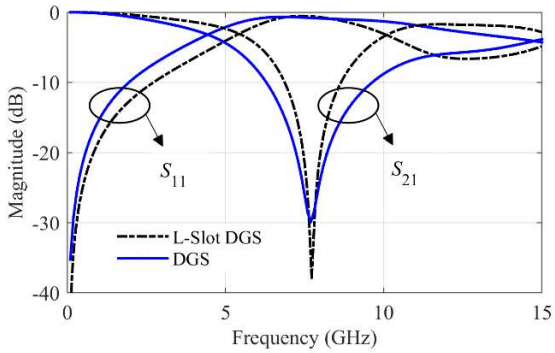

Fig. 3. *S*-parameters of microstrip lines showing resonance at 7.7 GHz.

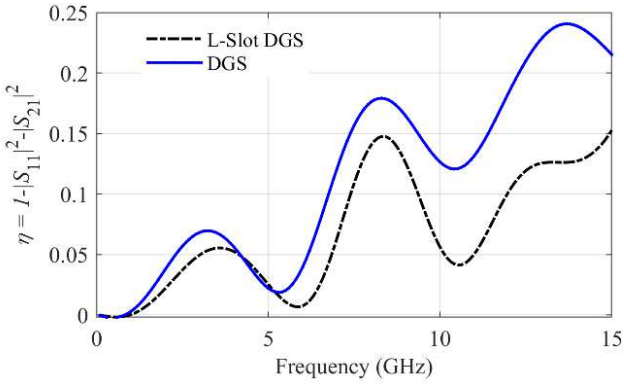

Fig. 4. Computed radiation rate factors. Both metallic and substrate losses are neglected for approximated computation.

Table I. Cell Design Parameters and Circuit Equivalence of the L-Slot DGS

Dimensions	*Value* (mm)	*Extracted Parameters*	*Value*
$a \times b$	3.0 × 3.0	Radiation resistance, R_{rad} (Ω)	100.0
g	0.2	Equivalent capacitance, C (pF)	0.2976
W	2.44	Equivalent inductance, L (nH)	1.44
W_L	0.6	Characteristic impedance, Z_0 (Ω)	50.0
Ls	2.8	Resonance frequency (GHz)	7.7
Ws	0.9	Capacitive operation (GHz)	10.4

Radiation loss of the L-Slot DGS is sensitive to the ratio W_L/W [11]. When choosing the ratio as low as 0.4, the current flow is concentrated beneath the line resulting in a dominant equivalent capacitive effect while field leakage from the backside plane is diminished. For instance, Fig. 4 shows a minimum radiation rate produced by the microstrip-type bandgap effect at 10.4 GHz, above resonant frequency (7.7 GHz). The L-Slot DGS unit-cell can be modeled by an equivalent LC circuit and extracted as a one-pole Butterworth lowpass filter as in Fig. 5*a*. For frequencies higher than cut-off frequency, it is necessary to include a frequency dependent resistance, R, which accounts esentially for radiation of the unit-cell structure de-embedded from the microstrip line. Thus, the equivalent susceptance, Y_e, can be written as [4]:

$$Y_e(\omega) = j\omega_0 C\left(\frac{\omega}{\omega_0} - \frac{\omega_0}{\omega}\right) + \frac{1}{R(\omega)} \quad . \tag{1}$$

For capacitively coupled filter design, the high-frequency circuit equivalence in Fig. 5*b* should be taken into account. The dominant capacitive effect and radiation resistance developed at frequencies above resonant, for instance at $2\omega_0$, are given, respectively as:

$$B_C = \mathrm{Im}\left(Y_e(2\omega_0)\right) = 3\omega_0 C/2\,, \tag{2}$$

$$R_{rad} = \mathrm{Re}\left(1/Y_e(2\omega_0)\right) = R(2\omega_0) \tag{3}$$

As shown later, the implementation of a series resonator for filter design is related to the susceptive capacitance in (2), whereas the radiation resistance is fixed for an allowed radiation rate.

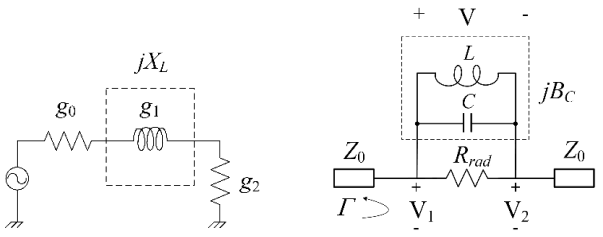

a) *b)*

Fig. 5. Broadband circuit-model equivalence of the L-Slot DGS unit-cell. (*a*) Extracted Butterworth-type one-pole lowpass equivalence [2], (*b*) High-frequency equivalence including radiation resistance at $2\omega_0$ ($B_C > 0$).

III. EM Performance

A. Shield Current Regulation

The additional inductance created by defected ground structures is explained by the magnetic current flowing along the unit-cell lattices. Fig. 6 depicts EM fields on the ground plane of the conventional structure and those of the L-Slot pattern at 10.4 GHz, above the resonant frequency. Fig. 6*a* also shows the return current tracing a path of least impedance to the source. An unneglectable current around the apertures is apparent. At such frequency, current must be concentrated below the microstrip line so as to develop an equivalent capacitive effect. However, the electric field trapped in the capacitive gap distance (g) is not strong enough to enforce current to travel along the microstrip line as a certain amount of current goes directly around unit lattices [13]. Such current path distribution sustains a magnetic current that produces mild field leakage from the ground plane.

Fig. 6*a* and Fig. 6*b* depict a higher electric field intensity in the narrow gap of the L-Slot DGS unit-cell when compared to that of the conventional pattern. Since both designs have the same gap distance, the conventional pattern exhibits a smaller equivalent capacitance. The L-Slot DGS provides the ratio W_L/W as a degree of freedom by which the capacitance can be increased and thus the resonant pole is shifted leftwards.

Owing to the microstrip-type defect added in the pattern, the path of least impedance on the ground plane changes with frequency. The additional bandgap takes place in a similar way to that in DMS structures. The strong electric field under the microstrip line results in an accumulated charge around the small distance in L-Slots (W_e, see Fig. 2) resulting in a capacitive effect. However, current cannot flow at minimal impedance around L-Slots as occurs at low frequencies because the created electric field in such a narrow gap is not strong enough to maintain a sufficient current path leading to an outer path to emerge. Since the amount of this path reduces with frequency, the current distribution leads to as an inductive effect. This results in a microstrip-type defect that can be modeled by a resonant parallel LC circuit [5]. Fig. 6*b* shows the perturbation created by L-Slots leading to a controlled magnetic current flow.

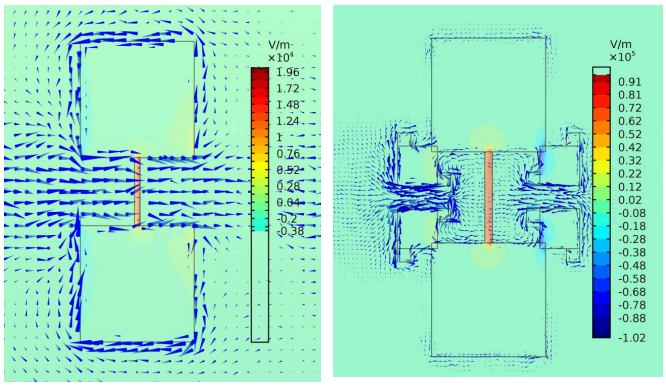

a) *b)*

Fig. 6. Backside view of simulated EM fields at 10.4 GHz, current density and electric field trapped in the gap. Conventional dumbell shaped pattern *a*), and DGS L-Slot pattern *b*).

B. Realized Gain

Radiation effects from the circuit area should be regulated for small insertion loss. Power loss is computed from the total gain (G_t) developed by the far-field lobes. The gain (G) of a given lobe is computed in orthogonal θ and φ components at its maximum radiation direction. The total gain is the sum of partial maximal gains; i.e. $G_t = G_{\theta,max} + G_{\varphi,max}$. 3D-EM simulation also was carried out to compute the realized gain (G_r) in terms of the impedance mismatch between the implicit radiation element of the microstrip line and the reference impedance resulting in the reflection coefficient, Γ. When assuming ideal conduction and dielectric efficiencies, the realized gain can be approximated by:

$$G_r \cong \left(1-\left|\Gamma\right|^2\right) G_t \,. \tag{4}$$

Radiation of the novel unit-cell occurs chiefly in the normal direction of the microstrip whereas a minimum amount of power leaks through the lattices etched on the ground plane [11]. The realized gain pattern of the L-Slot DGS structure is shown in Fig. 7 ("without PEC wall") and accounts for the case of the suspended microstrip line fully surrounded by absorbing conditions. Now, to gauge leakage through the ground plane, a wall of perfect electric conductor (PEC) is placed nearby the backside plane of the microstrip lines at distance d. The PEC plane has the same dimension than that of the ground plane ($L \times W_{\text{total}}$, see Fig. 2). Fig. 7 depicts the actual main beam and the virtual gain plane in the φ plane for both microstrip lines. The simulation results allow comparing realized gains when d is equal to the substrate height (H), with $H = 0.7874$ mm. At such distance, the reflected field in the PEC plane is added to direct fields in the actual plane thus intensifying radiation. This is more noticeable for the DGS case whereas the L-Slot DGS microstrip line achieves lower reflection in the PEC plane.

Table II lists normalized radiation power for the micostrip lines obtained by computing the reflection loss in (4). Fig. 8 shows approximated radiation power and total gain of the main lobe as a function of d.

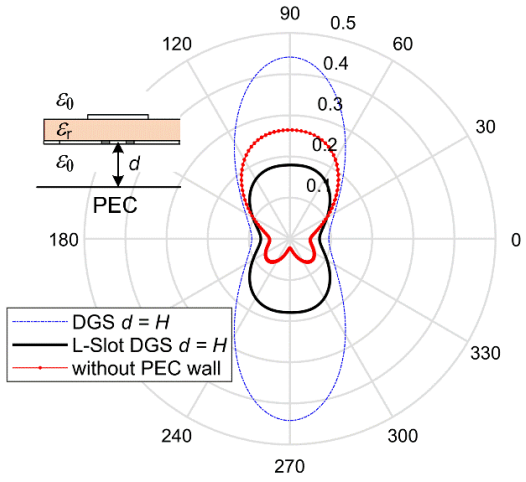

Fig. 7. Far-field realized gain (linear scale of the φ component) at propagation frequency 10.4 GHz. The virtual gain planes of suspended microstrip lines are displayed right below the bounded PEC conductor.

Table II. Microstrip Lines Radiation at 10.4 GHz (linear scale).

Case of study	*Realized gain*	*Total gain*	*Radiation loss power*
L-Slot DGS, without PEC wall	0.264	4.951	5.33×10^{-2}
L-Slot DGS, $d = H$	0.198	3.127	6.33×10^{-2}
DGS, $d = H$	0.4414	3.696	0.1194

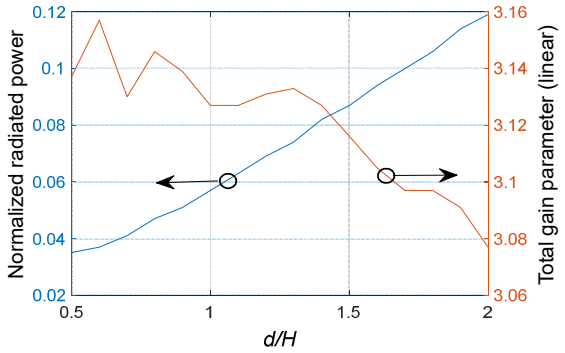

Fig. 8. Effect of placing a bounded PEC below the backside plane of the L-Slot DGS microstrip line.

Note from Table II that the novel unit-cell shows almost the same radiation loss when the separate PEC wall is placed at distance H and the case without the conductor wall. In contrast, the DGS microstrip line radiates twice as much power of the L-Slot DGS unit-cell. To some extent, higher radiation loss arises due to the implementation of large lattices area (3.5×3.5) mm^2.

Fig. 8 shows that the total gain presents low variation with distance whereas power coupling, hence radiated power present significant variation. According to these results, the PEC plane can be placed at certain distance from the ground plane to produce similar radiation power to that of the major lobe created by the structure fully surrounded by absorption condition. This suggests that for large distances, the PEC plane works mainly as a scatterer. Contriwise, for low distances, the main lobe power created by the capacitive gap discontinuity is reduced whereas more power is guided in the form of surface waves through the emerging waveguide formed by the PEC plane. A capacitive effect has to be included in the equivalent circuit model to take into account unwanted coupling of the PEC plane in close proximity with the microstrip ground plane.

C. Dissipated Power

When the PEC plane is replaced with a metallic wall for blinding field leakage, the balance of energy must include dissipated power due to the electric field, $\mathbf{E}_{\text{inc}}$, tangentialy incident on the induced current density vector, $\mathbf{J}_{\text{i}}$. Field leakage from the microstrip ground plane results in disipated power density (S_d). Power density averaged over a time period is given by [14]:

$$\left\langle S_d \right\rangle = \frac{1}{2}\,\text{Re}\left\{\mathbf{E}_{\text{inc}} \cdot \mathbf{J}_{\text{i}}^{*}\right\}. \tag{5}$$

To obtain the total power dissipated in a metallic wall of electrical conductivity (σ_c), the power density (5) is integrated over an area where the induced current density is confined. The dissipated power accounts for computing the current density penetrating into the conductor by a few skin depth. The skin depth (δ) below the metallic conductor surface is given by [14]:

$$\delta = \frac{1}{\sqrt{\pi f \mu_o \sigma_c}}, \tag{6}$$

where μ_o is the vacuum permeability constant. Fig. 9 displays the dissipated power of microstrip line's fied leakage at different frequencies and distances. Overall, results indicate that the microstrip line based on the L-Slot DGS unit-cell induces lower fields over the metallic wall and thus smaller dissipated power when compared with that of the DGS pattern. Fig. 10 depicts the induced fields in the metallic wall: the electric field intensity and the induced current density vector. Larger area of maximum magnitude of electical field is evident for the DGS structure. The metallic wall is separated by a distance H from the microstrip ground plane.

IV. BPF Filter Design

The filter design uses the capacitively-coupled resonator method to implement a BPF working at 10 GHz. Unlike previous BPF design showing bandpass at 10 GHz [12], our BPF uses L-Slot unit-cells to provide a wider stopband performance. Fig. 11 illustrates the proposed planar BPF structure, which is placed horizontaly over the metallic (copper-based) grounding wall and separated by 2.36 mm (= 3H) apart. Such distance is adequate to avoid the adverse influence of the metallic wall on filter responses, as assessed by parametric simulations. This information is useful for blinding excess electromagnetic radiation if the the planar filter is to be housed in a metal package.

The third-order BPF shown in Fig. 11 implements the input and output port (in-out) resonators with L-Slot DGS unit-cells. Each unit-cell is equally separated from the centered capacitive gap to set the filter bandpass frequency, $\omega_{0,\mathrm{BPF}}$. The resonators are $\lambda/2$ long at the center bandpass frequency and the design goal is accomplished by tuning the length of each microstrip line (ℓ). In a similar way to the half-wavelength capacitive-gap resonators [12], each unit-cell provides a specific capacitive susceptance, B_C at bandpass frequency so as to implement an admitance inverter. In reality, however, the resonator is influenced by the intrinsic radiation resistance of the L-Slot cell which impacts bandwidth and hence bandpass response. The design parameters are as follows. The self-resonance of unit-cells is chosen to be lower than the bandpass frequency. The gap discontinuity in the microstrip trace has a distance of 0.15 mm. For L-Slot DGS cells, the gap distance is 0.15 mm and lattice area (5.5 × 5.5) mm^2, which results in the attenuation-pole of the unit-cell located at 5.0 GHz. Fine tuning of the microstrip line results in ℓ = 6.67 mm and the central bandpass frequency at 10.57 GHz. Fig. 12 shows S-parameters of three-pole BPFs. The design that uses $\lambda/2$ capacitively-coupled resonators (dotted line) has center frequency and bandwidth equal to 9.75 GHz and 4.1 %, respectively. The other BPF is based on a single capacitive-gap and two L-Slot DGS sections. The banwidth of the response (solid line) is 12.3 % and center frequency of 10.57 GHz. The reponse is asymetric and exhibits a small roll-off factor because of the radiation resistance and the frequency dependent capacitance.

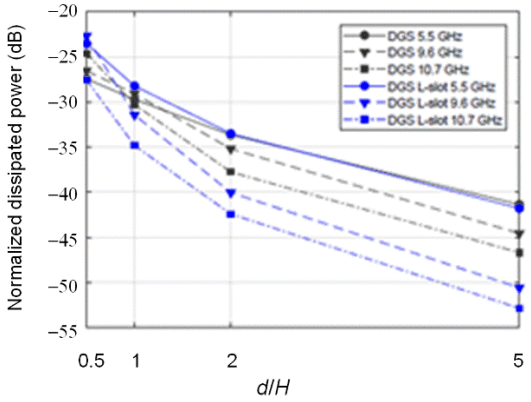

Fig. 9. Computed dissipated power in copper-based metallic wall.

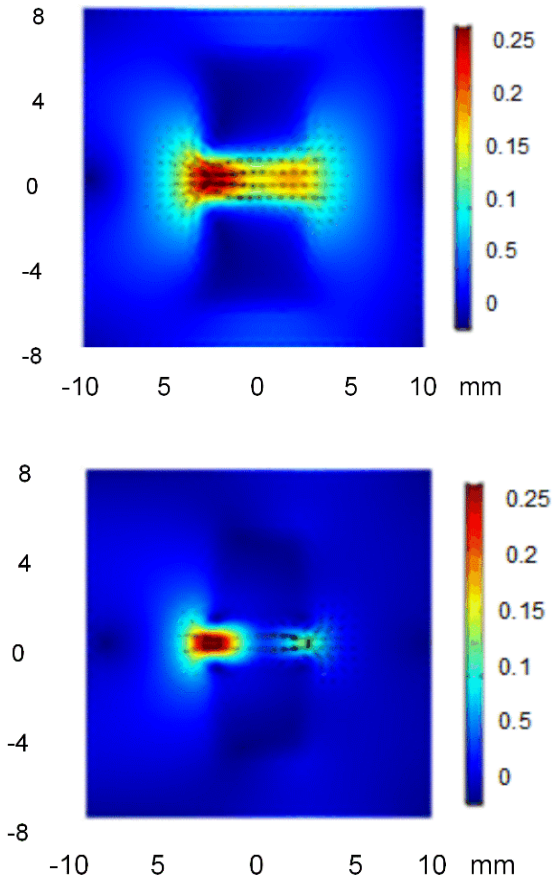

Fig. 10. E-field (V/m) and current density field (A/m^2) induced in the metallic wall at 10.4 GHz. DGS (upper) and L-Slot DGS (bottom).

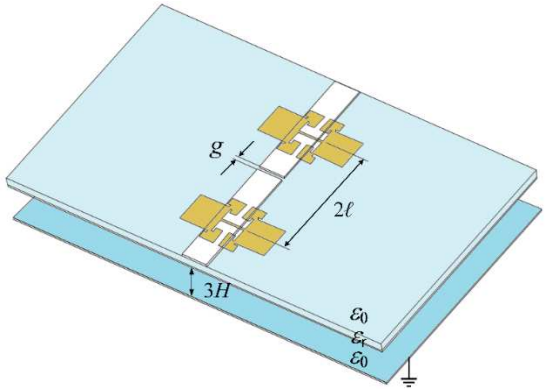

Fig. 11. 3D-view of the three-pole BFP. The distance of the centered gap discontinuity, *g*, is equal to 0.15 mm.

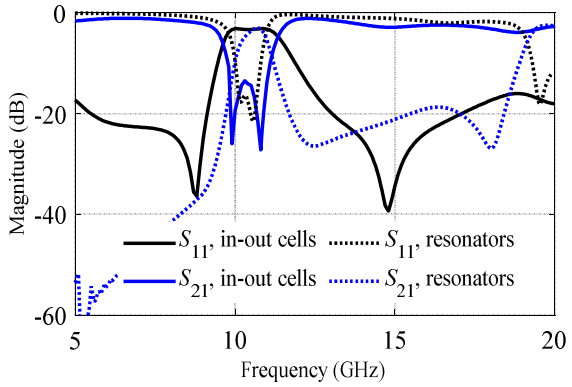

Fig. 12. Simulated *S*-parameters of microstrip BPFs.

Both designs have approximately the same intertion loss, about −3 dB. However, the implementation that regulates radiation losses through unit-cells attenuates the periodic response of the capacitively-coupled resonators (about 20 dB at 20 GHz) resulting in an improved upper bandstop response. This is because the field leakage control cannot be extended at frequencies reaching 20 GHz. In contrast, the BPF implementation with capacitive gaps shows a large second harmonic response.

V. CONCLUSIONS

This paper presents a new DGS-based BPF showing higher bandpass frequency when compared to previously reported demonstrations, some of them refered herein. The capacitive coupled unit-cell provides wider stopband performance above resonance. In addition, the control of return current enables to place nearby a metallic wall in order to improve the electromagnetic compatibility at the circuit level. The proposed structures can be designed using inexpensive printed circuit board fabrication and commercially available laminates. Measurements of the BPF are to be presented in a future paper.

REFERENCES

[1] K. Lim, S. Pinel, M. Davis, A. Sutono, C.-H. Lee, D. Heo, A. Obatoynbo, J. Laskar, E. Tantzeris and R. Tummala, "RF-System-On-Package (SOP) for Wireless Communications," IEEE Microwave Magazine, vol. 3, no. 1, pp. 88-99. March 2002.

[2] J. Coonrod, "Microstrip Defected Ground Structures Without Radiation Loss Using Multilayer PCB Technology," Microwave Journal,vol. 61, no.2, pp. 88-98, Feb. 2018.

[3] C. Kim, J. Park, D. Ahn, and J. Lim, "A Novel 1-D Periodic Defected Ground Structure for Planar Circuits," IEEE Microwave and Guided Wave Letters, vol. 10, no. 4, pp. 131-133, April 2000.

[4] D. Ahan, J. Park, C. Kim, J. Kim, Y. Qian, and T. Itoh, "A Design of the Low-Pass Filter Using the Novel Microstrip Defected Ground Structure," IEEE Transactions on Microwave Theory and Techniques, vol. 49, no. 1, pp. 86-93, 2001.

[5] M. K. Khandelawal, B. K. Kanaujia, and S. Kumar, "Defected Ground Structure: Fundamentals, Analysis, and Applications in Modern Wireless Trends," Review Article, Internation Journal of Antennas and Propagation, vol. 20, pp.1-22, February 2017.

[6] A. Kumar and K. Machavaram, "Microstrip Filter with Defected Ground Structure: A Close Perspective," International Journal Microwave Wireless Technology," vol. 5, no. 5, pp. 589-602, Octuber 2013.

[7] M. Kazerooni, A. Cheldavi, and M. Kamarei, "Analysis, Modeling, and Design of Cascaded Defected Microstrip Structure for Planar Circuits," RF and Microwave Computer-Aided Engineering, vol. 20, no. 2, pp. 170-181, 2010.

[8] J. Tirado-Mendez, H. Jardón-Aguilar, R. Flores-Leal, E. Andrade-Gonzalez, and F. Iturbide-Sanchez, "Improving Frequency Response of Microstrip Filters Using Defected Ground and Defected Micristrip Structures," Progress on Electromagnetics Research C, vol. 13, pp. 77-90, 2010.

[9] J. S. Park, J. S. Yun, and D. Ahn, "A Design of the Novel Coupled-Line Bandpass Filter Using Defected Ground Structure With Wide Stopband Performance," IEEE Transaction on Microwave Theory and Techniques, vol. 50, no. 9, pp. 2037-2042, September 2002.

[10] A. Boutejdar, A. Omar, and E. Burte, "High-Performance Wide Stop Band Low-Pass Filter Using a Vertically Coupled DGS-DMS-Resonators and Interdigitial Capacitor," Microwave and Optical Technology Letters, vol. 56, no. 1, pp. 87-91, January 2014.

[11] A. Abdel-Rahman, A. K. Verna, A. Boutejdar, and A.S. Omar, "Compact Stub Type Microstrip Bandpass Filter Using Defected Ground Plane," IEEE Microwave and Wireless Components Letters, vol. 14, no. 4, pp. 136-138, April 2004.

[12] A. Abdel-Rahman, et. al. "Control of Bandstop Response of Hi-Lo Microstrip Low-Pass Filter Using Slot in Ground Plane ," IEEE Transaction of Microwave Theory and Techniques, vol. 52, no. 4, pp. 1008-1011, April 2004.

[13] J. Aguilar-Torrentera, M. Hinojosa-Rivera, and J. Morales-Castillo, "A DGS Pattern Incluiding DMS Behaviour for Compact Unit-Cell Designs," IEICE Electronics Express, vol. 16, no. 1, pp. 1-8, January 10, 2019.

[14] R. E. Collin, "Foundations for Microwave Engineering," The IEEE Press Series on Electromagnetic Wave Theory, Wiley-Interscience, Second Edition, New York, 2001, pp. 617-626.

[15] N. C. Karmakar, S. M. Roy, and I. Balbin, "Quasi-Static Modeling of Defected Ground Structure," IEEE Transactions on Microwave Theory and Techniques, vol. 54, no. 5, pp. 2160–2168, May 2006.

[16] L. M. Magid, "Electromagnetic Fields, Energy and Waves," John Wiley&Sons, Fifth Edition, Michigan, 2010.